10-2020

Motion of phase boundary during antiferroelectric–ferroelectric transition in a PbZrO3-based ceramic

Binzhi Liu
Iowa State University, bzliu@iastate.edu

Xinchun Tian
Iowa State University

Lin Zhou
Iowa State University and Ames Laboratory, linzhou@ameslab.gov

Xiaoli Tan
Iowa State University and Ames Laboratory, xtan@iastate.edu

Motion of phase boundary during antiferroelectric–ferroelectric transition in a PbZrO3-based ceramic

Abstract

The *in situ* biasing transmission electron microscopy technique is employed to investigate the nucleation and growth of the ferroelectric phase during the electric field-induced phase transition in Pb0.99{Nb0.02[(Zr0.57Sn0.43)0.94Ti0.06]0.98}O3, a PbZrO3-based antiferroelectric ceramic. The first-order displacive phase transition is found to be highly reversible with the initial antiferroelectric domain configuration almost completely recovered upon removal of the applied field. In the forward transition from the antiferroelectric to ferroelectric phase, {100}c facets are dominant on the phase boundary; while in the reverse transition from the ferroelectric to antiferroelectric phase during bias unloading, the phase boundary is segmented into {101}c and {121}c facets. The motion of the phase boundary is nonuniform, taking the form of sequential sweeping of facet segments. The elastic distortion energy and the depolarization energy at the antiferroelectric/ferroelectric phase boundary is suggested to dictate the facet motion.

Disciplines

Engineering Physics | Materials Science and Engineering

Comments

This article is published as Liu, Binzhi, Xinchun Tian, Lin Zhou, and Xiaoli Tan. "Motion of phase boundary during antiferroelectric–ferroelectric transition in a PbZrO3-based ceramic." *Physical Review Materials* 4, no. 10 (2020): 104417. DOI: 10.1103/PhysRevMaterials.4.104417. Posted with permission.

Motion of phase boundary during antiferroelectric–ferroelectric transition in a $PbZrO_3$-based ceramic

Binzhi Liu,[1] Xinchun Tian,[1] Lin Zhou,[1,2] and Xiaoli Tan[1,*]

[1]*Department of Materials Science and Engineering, Iowa State University, Ames, Iowa 50011, USA*

[2]*Ames Laboratory, U.S. Department of Energy, Ames, Iowa 50011, USA*

(Received 26 July 2020; accepted 5 October 2020; published 29 October 2020)

The *in situ* biasing transmission electron microscopy technique is employed to investigate the nucleation and growth of the ferroelectric phase during the electric field-induced phase transition in $Pb_{0.99}\{Nb_{0.02}[(Zr_{0.57}Sn_{0.43})_{0.94}Ti_{0.06}]_{0.98}\}O_3$, a $PbZrO_3$-based antiferroelectric ceramic. The first-order displacive phase transition is found to be highly reversible with the initial antiferroelectric domain configuration almost completely recovered upon removal of the applied field. In the forward transition from the antiferroelectric to ferroelectric phase, $\{100\}_c$ facets are dominant on the phase boundary; while in the reverse transition from the ferroelectric to antiferroelectric phase during bias unloading, the phase boundary is segmented into $\{101\}_c$ and $\{121\}_c$ facets. The motion of the phase boundary is nonuniform, taking the form of sequential sweeping of facet segments. The elastic distortion energy and the depolarization energy at the antiferroelectric/ferroelectric phase boundary is suggested to dictate the facet motion.

DOI: 10.1103/PhysRevMaterials.4.104417

I. INTRODUCTION

The high energy storage density of antiferroelectric (AFE) oxides has revived worldwide interest in their fundamental research in recent years because of the urgent needs in high-performance capacitors [1–4]. In addition, AFE oxides are promising material candidates for high-strain actuators and electrocaloric cooling devices [5,6]. These applications of AFE materials all take advantage of the reversible first-order AFE ↔ ferroelectric (FE) phase transition. The prototype AFE compound is $PbZrO_3$ [2,7–9]; however, its field-induced AFE to FE phase transition has only been experimentally demonstrated in single crystals [10]. In polycrystalline $PbZrO_3$ ceramic at room temperature, the critical field for the phase transition, E_F, exceeds the breakdown strength of the ceramic. To reduce E_F for practical applications in devices, chemical modifications of $PbZrO_3$ have been extensively explored [11–17]. The reduction in E_F and the change of other electrical properties are attributed to the alteration of microstructures. Therefore, tailoring properties of AFE ceramics for specific target applications demands a full understanding of the structure-property relationships and the detailed revelation of the AFE ↔ FE phase transition process. Such knowledge will be equally applicable to the search of lead-free AFE materials to replace $PbZrO_3$-based compositions in the future [18–21].

In situ transmission electron microscopy (TEM) has been a powerful tool to study various nanoscale dynamic processes in AFE materials. Viehland *et al.* [22–24] reported that in tin-modified lead-zirconate-titanate ceramics, the AFE phase with incommensurate modulations transforms to an intermediate FE phase before it becomes the paraelectric phase during *in situ* heating. During *in situ* cooling, the wavelength of the incommensurate modulation decreases and eventually becomes commensurate in the AFE phase. Very recently, Wei *et al.* [25] reported an intermediate phase with cycloidal polarizations in $PbZrO_3$ triggered by electron beam radiation in TEM. Our group developed an *in situ* biasing TEM technique and has conducted detailed investigations on the evolution of satellite diffraction spots during the electric field-induced AFE to FE phase transition [26,27]. A structural model was inferred from the observation that the incommensurate modulation is an average effect of commensurate modulations with different wavelengths. However, these *in situ* TEM studies were quasistatic with biases applied discontinuously in a stepwise manner and electron diffraction patterns in reciprocal space were mainly examined and recorded. The detailed dynamic process of the AFE ↔ FE phase transition in real space, especially the nucleation/growth of the new phase and the motion of the phase boundary, remains unknown.

In the present work, a chemically modified $PbZrO_3$ ceramic was selected as a model system for fundamental investigation on the phase morphology change during the field-induced AFE ↔ FE transition. The nucleation and growth of the FE phase within the parent AFE phase are directly observed. The motion of the phase boundary, with $\{100\}_c$ (subscript c indicates pseudocubic notion) facets during the forward transition (AFE to FE) and with $\{101\}_c$ and $\{121\}_c$ facets during the reverse transition (FE to AFE), is recorded.

II. MATERIALS AND METHODS

A. Ceramic synthesis

The ceramic with a nominal chemical formula $Pb_{0.99}\{Nb_{0.02}[(Zr_{0.57}Sn_{0.43})_{0.94}Ti_{0.06}]_{0.98}\}O_3$, denoted as PNZST 43/6/2, was selected for the study because its

*Corresponding author: xtan@iastate.edu

E_F(~40 kV/cm) is readily achieved with the *in situ* TEM technique [15,28]. The ceramic was synthesized using the solid-state reaction method. Raw powders with high purity (≥99.9%) of PbO, Nb_2O_5, ZrO_2, SnO_2, and TiO_2 were weighed according to the chemical formula and mixed in a vibratory mill. 5% excess PbO powder was included to compensate for its evaporation loss in the subsequent calcination and sintering. The milled powder was calcined for 4 h at 850 °C to ensure phase purity and chemical homogeneity. The calcined powder was remilled and then sintered at 1300 °C for 3 h with $PbZrO_3$ (≥99.9%) as the protective powder in the double-crucible configuration.

B. TEM specimen preparation

The sintered ceramic was sliced and polished into a 3 mm×2 mm×20 μm thin plate and glued to a half-Cu-washer. A thin layer of gold was then sputtered on the ceramic plate and the sample was transferred to a copper mounting stub specifically designed for the Hysitron PI 95 STEM specimen holder using conductive silver paste (Chemtronics, cw2400). The stub piece, together with the sputtered gold film on the ceramic specimen, served as one electrode during the subsequent *in situ* TEM test. Six thin windows for the TEM experiment were milled from the edge of the ceramic plate using an FEI Helios focused ion beam (FIB) system with the following procedure: first, six carbon protective layers with the dimensions 15 μm×2 μm×2 μm were deposited on the side face of the ceramic plate at a current of 0.45 nA under 30 kV. Then, the material surrounding the six carbon pads was removed with FIB using large Ga-ion beam currents (21 nA or 9.2 nA) under 30 kV until a thickness of ~1 μm was reached for the membranes. These prethinned TEM specimens were further FIB-milled at progressively reducing beam currents (0.45 nA, 0.26 nA, 81 pA, and 23 pA) under 30 kV down to a thickness of ~120 nm. The TEM specimens were finally polished and cleaned to a thickness of ~100 nm at a beam current of 41 pA under 5 kV. The protective carbon layer was removed completely on some of the specimens during these steps. Figure 1(a) shows the six as-prepared TEM-ready specimens and Fig. 1(b) is a close-up view of one of them, with a size of 12 μm×10 μm×~100 nm. It should be noted that these TEM specimens were only attached to the ceramic plate on one side. The initially sputtered gold film on the ceramic plate served as an electrode in the following *in situ* TEM test, and the distance from the gold film edge to the outer edge of the specimen was used to estimate the nominal electric field.

C. *In situ* TEM experiments

The copper mounting stub with FIB-milled TEM specimens was loaded to a PI 95 single-tilt specimen holder. All grains close to the outer edge of the six TEM specimens were examined on an FEI Tecnai G2-F20 (S)TEM to identify those for which their low-index axes, such as $\langle 001\rangle_c$, $\langle 101\rangle_c$, or $\langle 111\rangle_c$, could be aligned to the electron beam direction with single-tilt. These grains were deemed suitable for subsequent *in situ* biasing TEM tests. One example of such grains along its $\langle 001\rangle_c$ zone axis is shown in Fig. 1(c). Consistent with

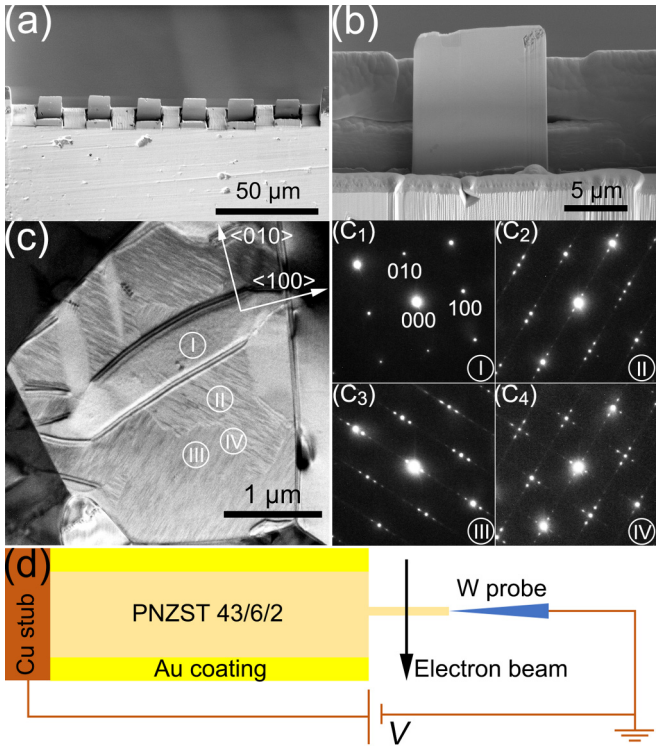

FIG. 1. Experimental procedure and *in situ* TEM test configuration. (a) and (b) SEM micrographs of ceramic thin windows fabricated using a focused ion beam (FIB) system. (c) Bright-field TEM micrograph of a grain along the $\langle 001\rangle_c$ zone axis showing coexisting ferroelectric domain (I) and antiferroelectric (AFE) domains (II and III). Area IV is at the wall between AFE domains II and III. (c_1) to (c_4) The selected area electron diffraction patterns corresponding to areas in (c). (d) Schematic diagram of the experimental configuration of the biasing *in situ* TEM study. The tungsten probe is grounded while the specimen is subjected to a positive voltage under the normal biasing condition.

previous studies [26–28], the grain contains AFE domains with fine fringes. Electron diffraction patterns from selected areas of I, II, III, and IV are displayed in Fig. 1(c_1) through (c_4), respectively. The presence of satellite diffraction spots in areas II, III, and IV is the fingerprint of the AFE phase with incommensurate modulations. The absence of satellite spots in Fig. 1(c_1) suggests that area I might be either in the FE phase or an AFE domain with inclined modulation slabs [28,29].

In situ biasing TEM experiments were conducted using the configuration schematically shown in Fig. 1(d). A sharp tungsten probe was positioned precisely to make electric contact on the edge of the TEM specimen. The tungsten probe was grounded while the specimen was connected to a positive voltage under the normal bias condition. Under a reverse bias loading, the specimen was connected to a negative voltage. In TEM specimens with the protective carbon layer completely cleaned away, the tungsten probe would make a point contact directly on the ceramic and generate nonuniform fields in the specimen. In specimens with some residuals of the protective carbon layer, a uniform electric field is expected when the tungsten probe contacts the carbon layer on the edge of

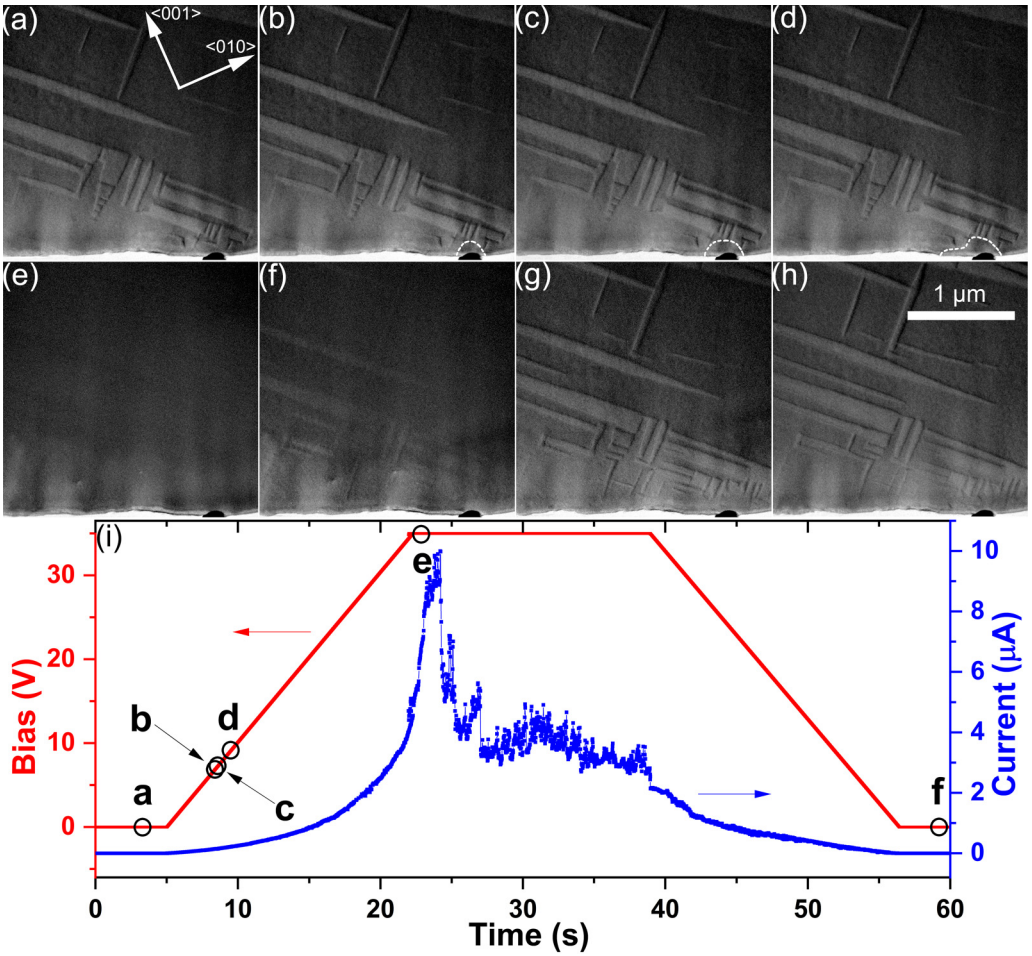

FIG. 2. Snapshots from the recorded video file (shown in the Supplemental Material [30]) demonstrating the reversible AFE-FE phase transition under nonuniform field. The grain of interest is observed along its $\langle 100 \rangle_c$ zone axis, and the dark object on the lower right edge is the tungsten probe tip. (a) $t = 3.3$ s, $U = 0.0$ V. This grain is in the AFE phase with multiple domains. (b) $t = 8.4$ s, $U = 6.9$ V. The bright dashed line marks the FE phase nucleus. (c) $t = 8.6$ s, $U = 7.3$ V. The FE nucleus expands into the AFE phase. (d) $t = 9.6$ s, $U = 9.3$ V. The upward growth of the FE phase is hindered by other AFE domains and the upper left growth is pinned by the defect in dark contrast. (e) $t = 22.9$ s, $U = 35.0$ V. General phase transition occurs within the whole viewing area. (f) $t = 40.0$ s, $U = 32.9$ V. The reverse phase transition starts during bias ramping down. (g) $t = 43.9$ s, $U = 25.1$ V. The reverse transition to the AFE phase is complete with almost all original AFE domains recovered. (h) $t = 59.1$ s, $U = 0.0$ V. Further growth of a few AFE domains. (i) The applied bias profile and the simultaneously recorded electric current. The snapshot micrographs in (a) through (h) are marked on the bias profile.

the specimen. A sourcemeter (Keithley 2602B) was connected to the PI 95 specimen holder to provide the voltage bias and record the electric current during *in situ* TEM experiments. The electric bias was applied in a continuous profile with three segments (ramp up, dwell, and ramp down) of roughly 17 s each.

III. RESULTS AND DISCUSSION

A. The reversible antiferroelectric ↔ ferroelectric phase transition

The *in situ* TEM experiment was first performed on a specimen subject to nonuniform electric fields with the tungsten-probe making a point electrical contact (no residual carbon protective layer on the side surface of the TEM specimen). The nominal applied field at the maximum biasing voltage (35.0 V) was ~38 kV/cm. In this specimen, a grain that can be imaged along the $\langle 100 \rangle_c$ zone axis was found on the edge and the *in situ* test results are displayed in Fig. 2. The voltage bias with a continuous profile is displayed in Fig. 2(i) and the evolution of the domain morphology is presented in the video clip in the Supplemental Material [30]. The electric current was simultaneously recorded and is also included in Fig. 2(i). Selected snapshots from the video file are presented in Figs. 2(a) through 2(h).

Figure 2(a) shows two sets of long and thin AFE domains prior to biasing, embedded in the matrix domain. The domain walls appear to be edge-on and are on $\{011\}_c$ planes. Previous research has shown that $PbZrO_3$ typically exhibits 90° AFE domains with $\{100\}_c$ walls, 60° AFE domains with $\{011\}_c$ walls, and 120° AFE domains with $\{011\}_c$ or $\{112\}_c$ walls [8,29,31–33]. In addition, the satellite diffraction spots from the grain of interest are almost invisible; therefore, the domains in Fig. 2 are most likely 60° AFE domains with Pb-cation displacements and the domain wall schematically shown in Fig. 3(a).

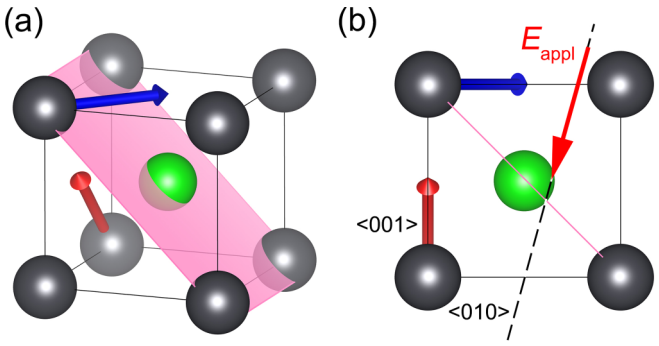

FIG. 3. (a) Schematic diagram showing the Pb-cation displacements and a 60° AFE domain wall (pink) in a pseudocubic perovskite unit cell with. Dark spheres stand for Pb, the green sphere represents the B-site cation, and O anions are omitted for clarity. (b) The projected view along the $\langle 100\rangle_c$ direction to represent the situation in Fig. 2, with the direction of the nominal applied field marked.

Figures 2(b), 2(c), and 2(d) show the nucleation of the FE phase (marked by the bright dashed curve) in the early stage of the AFE to FE phase transition. The nucleus of the induced FE phase initiates at the probe contact point in the form of a semicircle and rapidly grows outward into the AFE phase. When its radius reaches ~150 nm, the FE phase starts to grow preferentially to the left side [Fig. 2(d)]. It seems that growth toward the upper direction is resisted by the AFE domain wall. This could be explained by the different orientations of the Pb-cation displacements in the AFE domains across the domain wall, as schematically shown in Fig. 3(b). As a result, the driving forces in the AFE domains to rotate the Pb displacement toward the $\langle 111\rangle_c$ direction (the polar direction in the FE phase) is different. On the other hand, the growth to the upper left direction is pinned by a defect [in dark contrast adjacent to the phase boundary in Fig. 2(d)], producing a concave portion on the boundary. However, the resistance to the growth of the FE phase is easily overcome by further increase in the biasing voltage. At the end of the ramp when the bias reaches 35.0 V, all the AFE domains disappear and the whole viewing area transforms into the FE phase with a single domain [Fig. 2(e)].

In the meantime, the corresponding current increases gradually in the early ramping and then spikes to the major peak at the start of the bias dwelling, supporting the transition from the nonpolar AFE state to the polar FE state. The leakage current after the major peak during the bias dwelling displays a stochastic nature, indicating minor changes continuing in other grains in this specimen. The reverse phase transition (FE to AFE) appears to take place as the ramp down starts [Fig. 2(f)], and unfortunately, the AFE/FE phase boundary is hard to trace. The corresponding current abruptly decreases and then gradually disappears. It should be noted that a current peak in the opposite direction is expected to accompany the reverse transition. This is likely manifested as the abrupt reduction in the current value at $t = 38.9$ s when the ramp down begins. The absence of a peak with negative current values is possibly due to the resistive leakage current under the positive bias and the compensation of accumulated electrons from the electron beam. Further decrease in biasing voltage during ramp down leads to the reappearance of almost all the initial AFE domains, as shown in Fig. 2(g). Minor growth of a few AFE domains is further observed until the bias ramp down is complete [Fig. 2(h)].

The dynamic *in situ* observation seems to suggest that most AFE domains immediately form in the AFE phase resumed during the reverse transition. Additional AFE domains continue to nucleate and grow in the AFE phase even after the completion of the FE to AFE phase transition. The almost identical AFE domain patterns in Figs. 2(a) and 2(h) indicate not only the high reversibility of the AFE ↔ FE phase transition, but also the memory effect of those AFE domain walls. The reversible nature of the phase transition in PNZST 43/6/2 is consistent with the polarization measurement on bulk specimens and our previous *in situ* TEM experiments with a different specimen configuration [15,28].

B. The nucleation and growth of the ferroelectric phase

The nucleation and growth of the FE phase during the early stage of the AFE to FE transition was further investigated in another specimen, with a nominal applied field of ~33 kV/cm at the maximum biasing voltage (35.0 V). A grain on the edge of the specimen along its $\langle 001\rangle_c$ zone axis was observed and the results are displayed in Fig. 4. FIB specimen preparation cleaned the carbon protective layer away (hence nonuniform field in the grain) but seems to have produced damage along the edge, evidenced by the mottled contrast in Fig. 4(a). As shown in Fig. 4(b), the grain initially contains two AFE domains in the lower part and an FE domain in the upper right part (This FE domain might be an AFE domain with inclined modulation slabs). The nucleation of the FE phase out of the AFE II domain starts when the bias reaches 8.2 V and takes a mushroom shape at the contact point of the probe [Fig. 4(a)]. The narrower size of the FE nucleus at the surface edge implies the pinning effect from FIB-induced defects, the density of which rapidly decreases with distance from the surface region. As a result, the FE nucleus preferentially grows into the interior of the grain and gradually evolves into a circular shape [Figs. 4(b) and 4(c)]. The circular FE nucleus starts to develop facets on the AFE/FE phase boundary during further increase in biasing voltage [Figs. 4(d) and 4(e)]. At the maximum bias, facets become more apparent, following roughly the $\{100\}_c$ planes [Fig. 4(f)].

The radius of the circular FE nucleus before it shows facets is about 100 nm [Fig. 4(c)], which can be artificially set as the demarcation between nucleation and growth. Similar to the observations shown in Fig. 2, the wall between AFE domains I and II restricts the motion of the AFE/FE boundary. In Fig. 4(d), the upper left tip of the FE phase reaches the AFE domain wall. Further growth of the FE phase has pushed the AFE domain wall slightly upward, but the resistance apparently retards the vertical growth. In comparison, the growth in the horizontal direction does not experience any major blockage. Such an anisotropy in the FE phase growth is quantitatively displayed in Fig. 4(h). It is also evident that the AFE to FE phase transition is highly nonlinear: The nucleation stage completes in less than 1 s, while the growth stage initially proceeds rapidly and then slows down dramatically. In contrast to the grain shown in Fig. 2, the

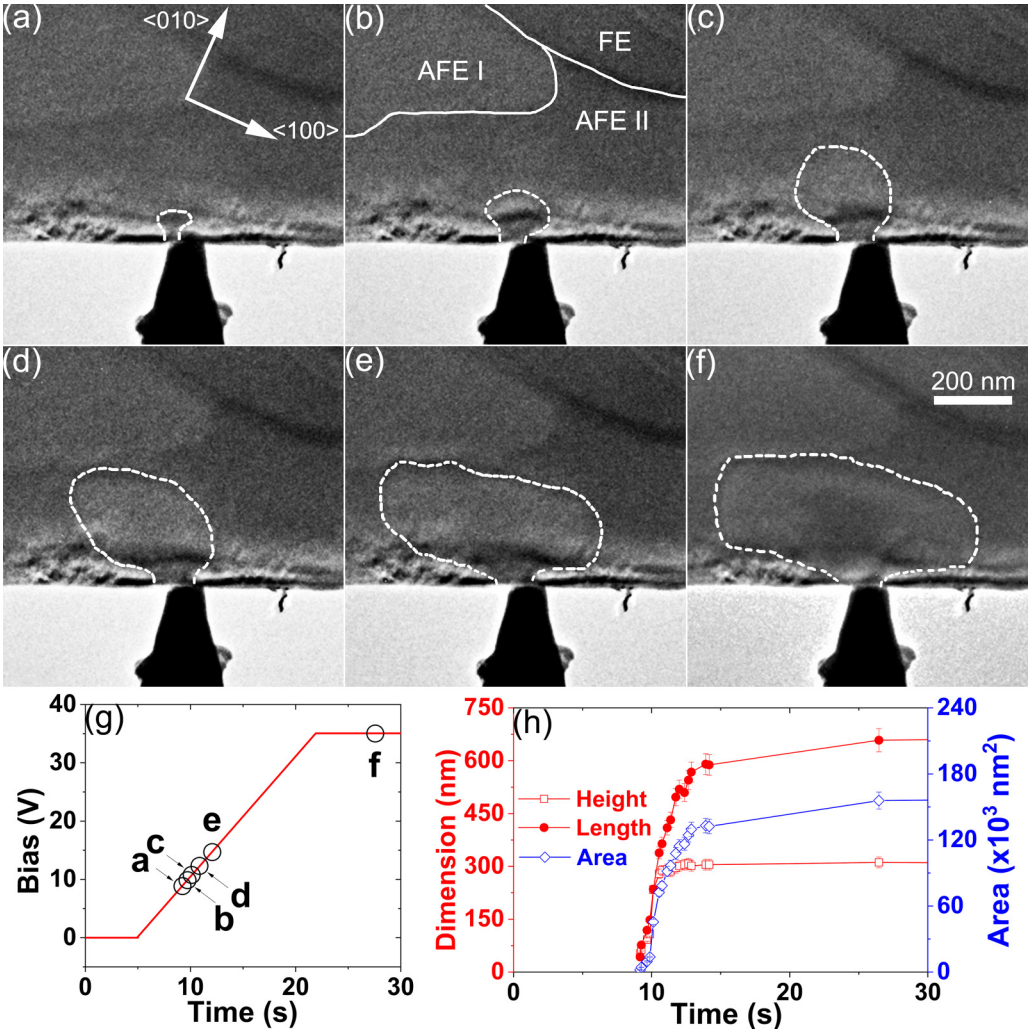

FIG. 4. Snapshots from the recorded video file on another grain observed along its $\langle 001 \rangle_c$ orientation to demonstrate the forward phase transition (AFE to FE) under nonuniform electric field. (a) $t = 9.3$ s, $U = 8.2$ V. The bright dashed line outlines the FE nucleus. (b) $t = 9.9$ s, $U = 9.3$ V. The FE nucleus expands. The bright solid lines in the upper part of the micrograph delineate the two AFE domains (I and II) and a coexisting FE domain. (c) $t = 10.1$ s, $U = 9.7$ V. The FE phase grows further with a circular phase boundary. (d) $t = 10.8$ s, $U = 11.0$ V. The FE phase grows preferentially toward the upper left and reaches the AFE domain wall. (e) $t = 12.9$ s, $U = 15.0$ V. The phase boundary starts to display facets while growth in the upper direction is hindered by the AFE domain wall. (f) $t = 27.8$ s, $U = 35.0$ V. The final configuration of the induced FE phase under the maximum applied voltage of 35.0 V. The facets are roughly along $\{100\}_c$ planes. (g) The profile of the applied bias where the corresponding snapshots are marked. (h) The height, length, and area of the induced FE phase measured from single frame micrographs of the video file. Abrupt growth is observed at around $t = 10$ s.

grain shown in Fig. 4 does not experience a complete AFE to FE transition, which is likely due to the presence of more FIB-produced defects as well as the different grain orientation with respect to the applied electric field. In addition, the nominal field is lower in the grain shown in Fig. 4 (33 vs 38 kV/cm).

C. Facets on moving antiferroelectric-ferroelectric phase boundaries

The facets on the AFE/FE phase boundary warrant further investigation. Their development during the growth of the induced FE phase implies the existence of crystallographic planes with minimum interfacial energy. In general, such compatible phase boundaries may hold the key to reducing the hysteresis and increasing the reversibility of displacive phase transitions [34,35]. In the case of boundaries separating AFE and FE phases, their energy has two primary components: elastic distortion energy due to the difference in lattice parameters, and depolarization energy due to the polar nature of the FE phase. Evaluating the elastic distortion energy requires detailed knowledge of crystal structure and elastic properties of both AFE and FE phases, which is beyond the scope of the present work. However, the situation can be greatly simplified if it is assumed that the lattice distortion in both phases is caused by Pb-cation displacement. When the AFE/FE interface is along $\{100\}_c$ and passes through the plane with only B-site cations and O anions (i.e., the midplane of

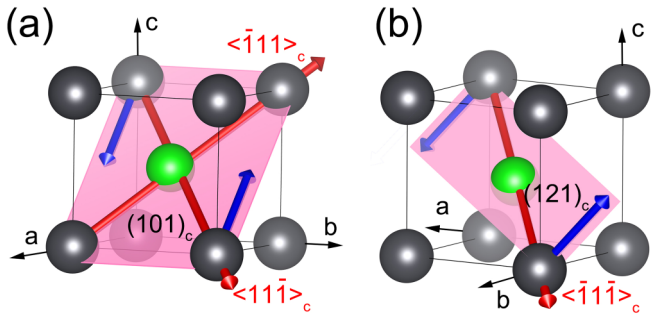

FIG. 5. Candidate crystallographic planes for AFE/FE phase boundary with minimum depolarization energy. (a) The $(101)_c$ plane contains in-plane $[10\bar{1}]_c$ and $[\bar{1}01]_c$ vectors (blue arrows) for Pb-cation displacements in the AFE phase and in-plane $[\bar{1}11]_c$ and $[11\bar{1}]_c$ vectors (red arrows) for Pb-cation displacements in the FE phase. (b) The $(121)_c$ plane contains in-plane $[10\bar{1}]_c$ and $[\bar{1}01]_c$ vectors (blue arrows) for Pb-cation displacements in the AFE phase and in-plane $[11\bar{1}]_c$ vector (red arrow) for Pb-cation displacements in the FE phase. The dark spheres stand for Pb, the green sphere represents a B-site cation, and O anions are omitted for clarity.

the pseudocubic perovskite unit cell), the mismatch strain at the interface could be at a minimum, because no Pb cations are on the interface. This suggests that $\{100\}_c$ planes are the candidates for the AFE/FE phase boundary with minimized elastic distortion energy. The observation of the $\{100\}_c$ facets in Fig. 4 seems to support this argument.

Special crystallographic planes with minimized depolarization energy can also be deduced [28]. In the AFE phase in $PbZrO_3$-based ceramics, the dipoles are antiparallel and are primarily from the Pb-cation displacements along the $\{110\}_c$ directions [2,7,29]. The induced FE phase is rhombohedral with polar vectors along the $\langle 111\rangle_c$ directions [12,28,36,37]. In the pseudocubic perovskite structure, $\{101\}_c$ and $\{121\}_c$ are the only two families of planes that can contain both $\langle 110\rangle_c$ and $\langle 111\rangle_c$ directions in-plane (Fig. 5). The depolarization energy on such a phase boundary would be minimal. Therefore, $\{101\}_c$ and $\{121\}_c$ planes are candidates for facets on the AFE/FE phase boundary in $PbZrO_3$-based oxides.

In the search for prominent facets on AFE/FE phase boundaries in PNZST 43/6/2, it is noticeable that they are more likely to appear in specimens with residuals of the carbon protective layer on the edge. In these specimens, uniform electric fields are expected in the grain of interest since the tungsten-probe and the residual carbon layer act together as one electrode.

1. $\{100\}_c$ *facets*

More prominent $\{100\}_c$ facets are observed during the forward transition (AFE to FE) in a specimen with the residual protective carbon layer. A uniform electric field with a nominal value of ~32 kV/cm is expected at the maximum bias (35.0 V). The grain of interest has its $\langle 001\rangle_c$ zone axis along the electron beam direction and contains both AFE and FE phases prior to biasing [Fig. 6(a)]. A complex interphase boundary containing multiple segments divides the grain into a large AFE domain in the upper half, a small AFE domain in the center marked by the dark triangle, and the large area

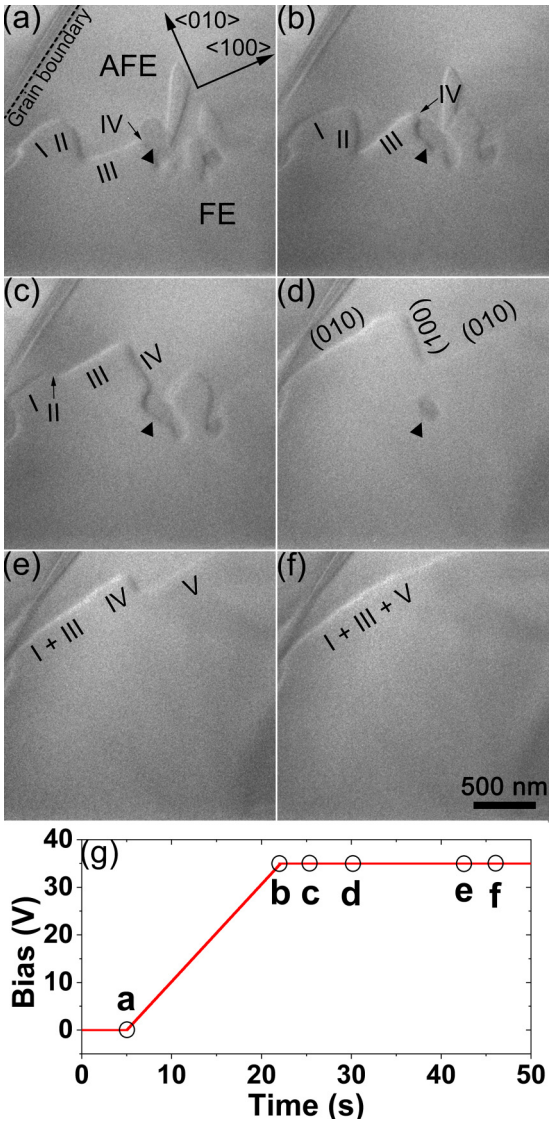

FIG. 6. Snapshots from the recorded video file on the third $\langle 001\rangle_c$-oriented grain reveal strong $\{100\}_c$ faceting on AFE/FE phase boundary during forward transition under uniform electric field with downward direction. (a) $t = 5.0$ s, $U = 0.0$ V. The grain initially has coexisting FE phase (lower part) and AFE phase (upper part) with a rough and complex phase boundary. The dark dashed line in the upper left corner marks a grain boundary. Symbols I, II, III, IV indicate different segments of the phase boundary. The dark triangle in the middle denotes a small AFE domain. (b) $t = 22.0$ s, $U = 35.0$ V. Segment III makes the largest advancement. (c) $t = 25.4$ s, $U = 35.0$ V. Again, Segment III moves farther and the small AFE domain seems to block the interphase boundary motion. (d) $t = 30.3$ s, $U = 35.0$ V. The complex interphase boundary straightens into three segments while the small AFE domain is fully enclosed in the FE phase. (e) $t = 42.5$ s, $U = 35.0$ V. The newly formed segment V moves rapidly. (f) $t = 45.9$ s, $U = 35.0$ V. All phase boundary segments merge to become a long straight boundary. (g) The profile of the applied bias where the corresponding snapshots are marked.

in the lower half for the FE phase. Initially, segments I and III are roughly on the $(010)_c$ planes, while segments II and IV follow the $(100)_c$ planes. The motion of the interphase boundary upward during dwelling at 35.0 V involves further

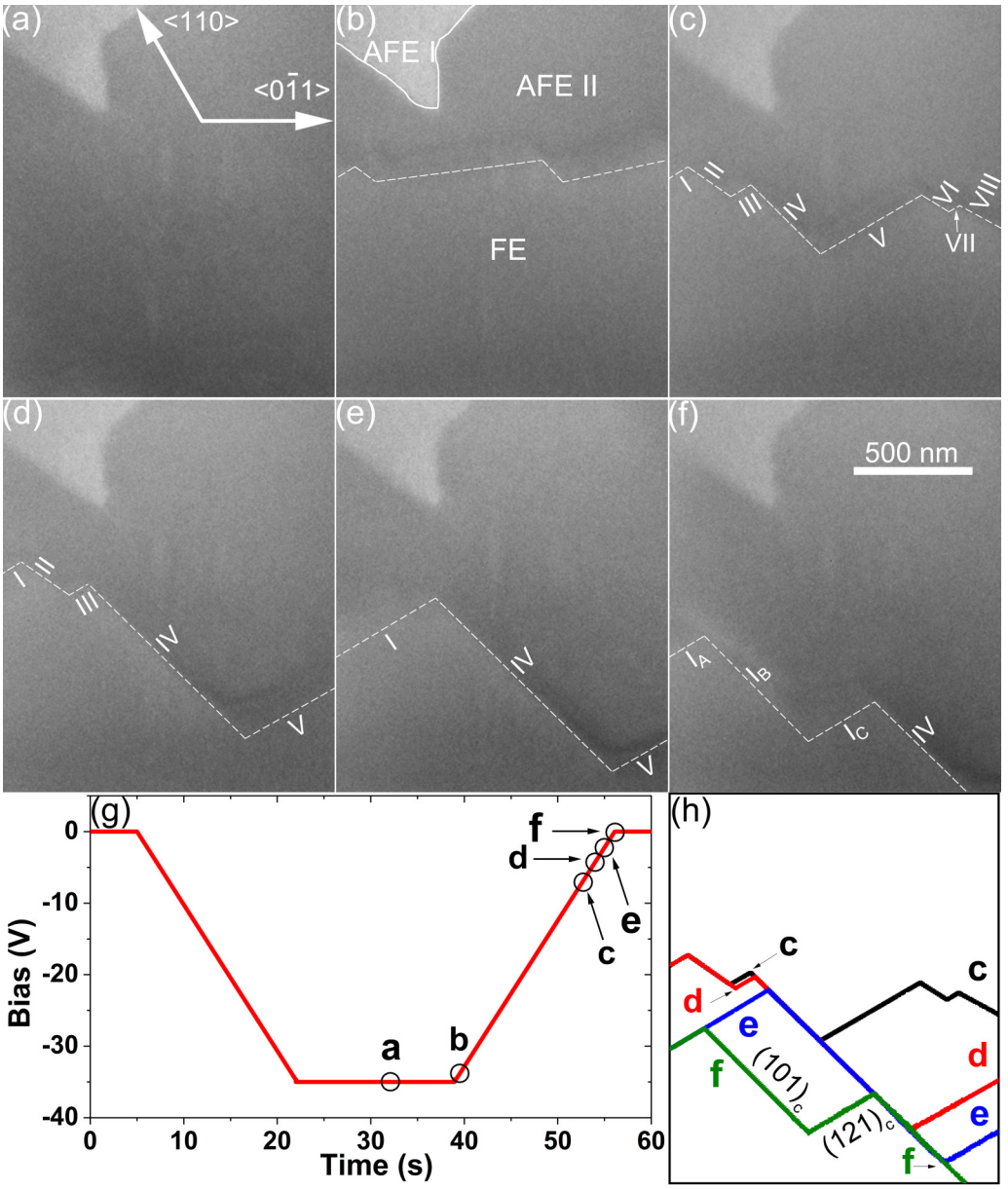

FIG. 7. Snapshots from the recorded video file on a $[\bar{1}11]_c$-oriented grain illustrate strong $\{101\}_c$ and $\{121\}_c$ faceting on the AFE/FE phase boundary during the reverse transition (FE to AFE). The applied electric field is uniform with the direction pointing upward. (a) $t = 31.9$ s, $U = -35.0$ V. The forward phase transition (AFE to FE) is about to occur. (b) $t = 39.6$ s, $U = -33.6$ V. The induced FE phase reaches maximum volume. The upper part of the micrograph shows two AFE domains, and the induced FE phase displays a faceted boundary. (c) $t = 52.6$ s, $U = -7.1$ V. The induced FE phase reverts to the AFE phase. Symbols I, II, III, IV, V, VI, VII, VIII denote the various segments along the interphase boundary. Preference on $\{101\}_c$ faceting (edge-on) and $\{121\}_c$ faceting (inclined) on the phase boundary is noticed. (d) $t = 53.9$ s, $U = -4.4$ V. Segment V of inclined $\{121\}_c$ facet moves quickly toward the lower right direction. (e) $t = 55.0$ s, $U = -2.2$ V. Segment I merges with segment III with segment II consumed. (f) $t = 56.0$ s, $U = 0.0$ V. Part of segment I (I_C) breaks out and moves rapidly toward the lower right direction. (g) The profile of the applied bias where the corresponding snapshots are marked. (h) The interphase boundary contours are overlaid, with symbols c, d, e, f corresponding to those shown in (c), (d), (e), and (f), respectively.

development of these $\{100\}_c$ facets [Figs. 6(b) through 6(f)]. In Fig. 6(b), segment III climbs around the small AFE domain, which seems to resist the interphase boundary motion. After segment IV on the $(100)_c$ plane surpasses the small AFE domain in the center, it extends and moves toward the $\langle 100\rangle_c$ direction [Fig. 6(c)]. The small AFE domain shrinks in size. Meanwhile, segments I and III on $(010)_c$ planes move forward along its normal directions at the expense of segment II on the $(100)_c$ plane. Segment II is completely consumed and disappears in Fig. 6(d) due to the motion of segments I and III, creating a long $(010)_c$ facet on the interphase boundary. The small AFE domain is now fully enclosed inside the growing FE phase, and a new $(010)_c$ facet, segment V, forms in the right part of the phase boundary. The embedded AFE domain completely transforms into the FE phase in Fig. 6(e). The newly formed segment V moves faster and catches up with

the combined I+III segment, consuming the whole segment IV and forming a very long $(010)_c$ facet [Fig. 6(f)].

The *in situ* TEM results in Fig. 6 not only verify the presence of $\{100\}_c$ facets on the AFE/FE phase boundary, but also reveal a higher mobility of $(010)_c$ facets than $(100)_c$ ones. The difference in mobility is likely a manifestation of different interfacial energies on the facets. Because the crystal structure of both AFE and FE phases is close to the highly symmetric cubic structure, the elastic distortion energy on $(010)_c$ and $(100)_c$ facets should be similar, if not the same. The difference in depolarization energy is then suggested to account for the different facet mobility. The electric field from the applied bias will alter the depolarization field to different extents on $(010)_c$ and $(100)_c$ facets; consequently, the depolarization energy of the $(010)_c$ facet is lower than the $(100)_c$ facet. As it moves, it will polarize the cations and anions in adjacent regions to a lesser degree and experience a lower resistance. Therefore, the $(010)_c$ facet exhibits a higher mobility than the $(100)_c$ facet.

2. $\{101\}_c$ *and* $\{121\}_c$ *facets*

In another specimen with a residual carbon protective layer on the edge, $\{101\}_c$ and $\{121\}_c$ facets are observed during the reverse transition (FE to AFE) in the ramp down of a negative bias (Fig. 7). The uniform field in the $[\bar{1}11]_c$-oriented grain is estimated to have a nominal value of ∼35 kV/cm at the peak bias. This grain is constituted with a small AFE domain (I) at the upper left corner and a large AFE domain (II) in the rest of the viewing area. After an incubation period for the whole dwelling stage of the bias, the lower part of AFE II abruptly transforms into the FE phase with a jagged interphase boundary [highlighted with bright dashed lines in Fig. 7(b)]. The faint fringe contrast along the boundary indicates the interface segments are inclined with respect to the electron beam.

As the bias ramps down, the reverse transition (FE to AFE) takes place through retracting the phase boundary. Initial retraction makes the phase boundary complex with eight segments in the viewing area [Fig. 7(c)]. Accurately determining the plane indices of these segments turns out to be difficult because of blurred contrast and not being on exact zone axis, even for major segments, such as IV and V in Fig. 7(c). Within an error range of 10°, segment IV is indexed to be an edge-on $(101)_c$ facet, while segment V is an inclined $(121)_c$ facet. As shown in Fig. 5, these planes are favored for their minimized depolarization energy.

The retraction of the phase boundary during the FE to AFE transition as the applied bias ramps down is realized through sequentially sweeping $(121)_c$ facets across the FE phase [Figs. 7(c)–7(f)]. Those short segments [I, III, and VII in Fig. 7(c)] appear to be seeds of the $(121)_c$ facet. In sequence from the right to the left side of the viewing area, they grow or merge, and then quickly move to the lower right through the FE phase. For example, in Fig. 7(d), segment V is the sweeping facet, stretching segment IV, merging with segment VII, and consuming segments VI and VIII. In Fig. 7(e), segment I merges with segment III at the expense of segment II. In Fig. 7(f), segment V moves out of the area while segment I splits into three shorter segments (I_A, I_B, I_C), with one (I_C) sweeping through the FE phase. The contours of the phase boundaries in Figs. 7(c)–7(f) are superimposed in Fig. 7(h), clearly revealing the rapid motion of $(121)_c$ facets during the FE to AFE transition.

It should be noted that the reverse transition continued in this specimen after the applied bias reached zero and completed in 5 s. At this stage without any applied field, there are only $(101)_c$ facets and $(121)_c$ facets on the phase boundary, with the former not moving. The self-sustaining motion of the $(121)_c$ facets (segments I_A and I_C) under zero applied field seems to suggest that their motion is driven by the depolarization energy. At the same time, the significant extension of the $(101)_c$ facet seems to hint at their low interfacial energy. Therefore, it is proposed that the $(101)_c$ plane is a unique interface with minimized depolarization energy [see Fig. 5(a)]. The particular Pb-cation displacements in the AFE and the FE phases across the phase boundary are out-of-plane with respect to $(121)_c$, and the resulting depolarization energy pushes the $(121)_c$ facet out of the crystal.

IV. CONCLUSIONS

The nucleation and growth of the ferroelectric phase during the electric field-induced phase transition is observed in real time in real space with the *in situ* TEM technique. In the antiferroelectric polycrystalline PNZST 43/6/2 ceramic, the ferroelectric nucleus initially takes a circular shape and starts to develop facets after its radius reaches ∼100 nm. The facets on the antiferroelectric/ferroelectric phase boundary are to reduce the elastic distortion energy and the depolarization energy. In the transition from the antiferroelectric to ferroelectric phase, $\{100\}_c$ facets are often observed; while in the reverse transition during ramping down of applied voltage bias, $\{110\}_c$ and $\{112\}_c$ facets are favored. The phase boundary advances or retracts through discontinuous motion of facet segments. These observations may also hold true for the antiferroelectric-ferroelectric phase transition in other perovskite compositions.

ACKNOWLEDGMENTS

This work was supported by the USA National Science Foundation (NSF) through Grant No. DMR-1700014. All electron microscopy work was performed at the Sensitive Instrument Facility at the U.S. DOE Ames Laboratory.

[1] S. Kwon, W. Hackenberger, E. Alberta, E. Furman, and M. Lanagan, IEEE Electr. Insul. Mag. **27**, 43 (2011).

[2] X. Hao, J. Zhai, L. B. Kong, and Z. Xu, Prog. Mater. Sci. **63**, 1 (2014).

[3] A. Chauhan, S. Patel, R. Vaish, and C. Bowen, Materials **8**, 8009 (2015).

[4] L. Yang, X. Kong, F. Li, H. Hao, Z. Cheng, H. Liu, J. Li, and S. Zhang, Prog. Mater. Sci. **102**, 72 (2019).

[5] W. Y. Pan, C. Q. Dam, Q. M. Zhang, and L. E. Cross, J. Appl. Phys. **66**, 6014 (1989).
[6] B. Lu, P. Li, Z. Tang, Y. Yao, X. Gao, W. Kleemann, and S.-G. Lu, Sci. Rep. **7**, 45335 (2017).
[7] F. Jona, G. Shirane, F. Mazzi, and R. Pepinsky, Phys. Rev. **105**, 849 (1957).
[8] D. I. Woodward, J. Knudsen, and I. M. Reaney, Phys. Rev. B **72**, 104110 (2005).
[9] A. K. Tagantsev, K. Vaideeswaran, S. B. Vakhrushev, A. V. Filimonov, R. G. Burkovsky, A. Shaganov, D. Andronikova, A. I. Rudskoy, A. Q. R. Baron, H. Uchiyama, D. Chernyshov, A. Bosak, Z. Ujma, K. Roleder, A. Majchrowski, J.-H. Ko, and N. Setter, Nat. Commun. **4**, 2229 (2013).
[10] O. E. Fesenko, R. V. Kolesova, and Y. G. Sindeyev, Ferroelectrics **20**, 177 (1978).
[11] D. Viehland, D. Forst, and J.-F. Li, J. Appl. Phys. **75**, 4137 (1994).
[12] S.-E. Park, M.-J. Pan, K. Markowski, S. Yoshikawa, and L. E. Cross, J. Appl. Phys. **82**, 1798 (1997).
[13] D. Forst, J.-F. Li, Z. Xu, and D. Viehland, J. Am. Ceram. Soc. **81**, 2225 (1998).
[14] T. Asada and Y. Koyama, Phys. Rev. B **69**, 104108 (2004).
[15] H. He and X. Tan, J. Phys.: Condens. Matter **19**, 136003 (2007).
[16] Z. Dai, Z. Xu, and X. Yao, Appl. Phys. Lett. **92**, 072904 (2008).
[17] Z. Liu, X. Chen, W. Peng, C. Xu, X. Dong, F. Cao, and G. Wang, Appl. Phys. Lett. **106**, 262901 (2015).
[18] Y. Guo, M. Gu, H. Luo, Y. Liu, and R. L. Withers, Phys. Rev. B **83**, 054118 (2011).
[19] H. Shimizu, H. Guo, S. E. Reyes-Lillo, Y. Mizuno, K. M. Rabe, and C. A. Randall, Dalton Trans. **44**, 10763 (2015).
[20] L. Zhao, Q. Liu, J. Gao, S. Zhang, and J.-F. Li, Adv. Mater. **29**, 1701824 (2017).
[21] P. Fan, S.-T. Zhang, J. Xu, J. Zang, C. Samart, T. Zhang, H. Tan, D. Salamon, H. Zhang, and G. Liu, J. Mater. Chem. C **8**, 5681 (2020).
[22] Z. Xu, D. Viehland, P. Yang, and D. A. Payne, J. Appl. Phys. **74**, 3406 (1993).
[23] D. Viehland, Phys. Rev. B **52**, 778 (1995).
[24] Z. Xu, D. Viehland, and D. A. Payne, J. Mater. Res. **10**, 453 (1995).
[25] X.-K. Wei, C.-L. Jia, H.-C. Du, K. Roleder, J. Mayer, and R. E. Dunin-Borkowski, Adv. Mater. **32**, 1907208 (2020).
[26] H. He and X. Tan, Phys. Rev. B **72**, 024102 (2005).
[27] H. Guo and X. Tan, Phys. Rev. B **91**, 144104 (2015).
[28] Z. Fan, F. Xue, G. Tutuncu, L.-Q. Chen, and X. Tan, Phys. Rev. Appl. **11**, 064050 (2019).
[29] M. Tanaka, R. Saito, and K. Tsuzuki, Jpn. J. Appl. Phys. **21**, 291 (1982).
[30] See Supplemental Material at http://link.aps.org/supplemental/10.1103/PhysRevMaterials.4.104417 for a movie clip showing the reversible AFE ↔ FE phase transition.
[31] G. J. Shen and K. Shen, J. Mater. Sci. **34**, 5153 (1999).
[32] J. Ricote, R. W. Whatmore, and D. J. Barber, J. Phys.: Condens. Matter **12**, 323 (2000).
[33] Z. Fan, T. Ma, J. Wei, T. Yang, L. Zhou, and X. Tan, J. Mater. Sci. **55**, 4953 (2020).
[34] J. Cui, Y. S. Chu, O. O. Famodu, Y. Furuya, J. Hattrick-Simpers, R. D. James, A. Ludwig, S. Thienhaus, M. Wuttig, Z. Zhang, and I. Takeuchi, Nat. Mater. **5**, 286 (2006).
[35] Y. Song, X. Chen, V. Dabade, T. W. Shield, and R. D. James, Nature (London) **502**, 85 (2013).
[36] C. T. Blue, J. C. Hicks, S. E. Park, S. Yoshikawa, and L. E. Cross, Appl. Phys. Lett. **68**, 2942 (1996).
[37] H. He and X. Tan, Appl. Phys. Lett. **85**, 3187 (2004).